Fifth European Conference on Computational Fluid Dynamics
ECCOMAS CFD 2010 (June 14 - 17, 2010).

A numerical simulation of axisymmetric ICP torches.

S. Clain[1], D. Rochette[2], R. Touzani[3], M. Lino da Silva[4], D. Vacher[2], P. André[2]

[1] *Institut de Mathématiques, CNRS UMR 5219, Université Paul Sabatier, Toulouse, France*

[2] *Clermont Université, Université Blaise Pascal, LAEPT, BP 10448, F-63000 CLERMONT-FERRAND*
CNRS, FRE 3120, LAEPT, F-63177 AUBIERE

[3] *Clermont Université, Université Blaise Pascal, Laboratoire de Mathématiques, BP 10448, F-63000 CLERMONT-FERRAND*
CNRS, UMR 6620, LM, F-63177 AUBIERE

[4] *Instituto de Plasmas e Fusão Nuclear, Laboratório Associado, Instituto Superior Técnico, Av. Rovisco Pais, 1049-001 Lisbon, Portugal*

1 Introduction

Atmospheric pressure Inductively Coupled Plasma (ICP) torches are long lived and stable plasma sources which are useful for a wide range of scientific and industrial applications. Among these we can cite applications such as waste treatment, monitoring of pollutants [1], testing of ablative and heat-resistant materials in the scope of atmospheric entry studies [2, 3], or spectroscopy applications [4, 5].

Such applications require a precise knowledge of the physical-chemical properties of these plasmas, and therefore a great number of complementary investigations are carried out regarding the experimental characterization and the numerical modelling of such plasma sources. This not only allows gaining a proper insight of the importance of the different physical-chemical processes in such plasmas, but more importantly it allows gaining a predictive insight on such plasmas.

Plasma torch modeling represents a challenging complex multiphysics problem. Hydrodynamics, electromagnetics and radiative transfer are the three basic ingredients which are involved in the mathematical model where numerical schemes have to be specifically designed to take the strong coupling into account. The goal of the present contribution is to show with a simple example that the choice of the numerical scheme has a critical impact in the ICP simulation: roughly speaking we can obtain two definitely different solutions for the same problem using two different solvers which brings into question a blind usage of numerical solvers proposed (for example) in commercial packages.

In this work, we consider the ICP-T64 plasmas torch [6] operated in the Laboratoire Arc Electrique et Plasmas Thermiques. This classical ICP torch is able to work with different kinds of plasma gas (air, argon, CO_2, N_2 and gas mixtures). This inductively coupled plasma system operates at a frequency of 64 MHz. A seven-turn induction coil, cooled by air, is used to ignite and sustain the plasmas of different gas mixtures. The plasma is generated through the induction coil by a radio frequency (RF) of 64 MHz delivering a power up to 3 kW. The plasma is confined within a 28 mm quartz tube. The plasma gas is injected at a fixed rate of more than 5 L/min.

2 Mathematical modeling and numerical method

Plasma torch simulation couples three kinds of physical phenomena: Fluid mechanics, electromagnetism and radiation transfer leading to a complex and intricate multiphysics problem. The Navier-Stokes equations govern the fluid motion while the Maxwell system describes the electromagnetic fields evolution. Strong couplings arise between the two systems. Indeed the plasma conductivity depends on the plasma temperature while the heating of the fluid is driven by the Joule heating source induced by the electric field and by the radiation transfer. In addition, the fluid motion (gas and plasma) is driven by the Lorentz force.

2.1 The modeling

In order to take advantage of axisymmetric geometries we use cylindrical coordinates (r, θ, z) with θ–invariance, and make the following simplifying assumptions (see Fig. 1-left):

i) Viscosity and thermal diffusion of the gas are neglected,

ii) Electric and magnetic fields are time-harmonic complex functions of angluar frequency ω,

iii) Displacement currents are neglected.

The symmetry implies moreover $E_r = E_z = 0$ and $H_\theta = 0$. This implies that the Lorentz force has the form $\mathbf{F}_L = (f_r, 0, f_z)$. Let us mention that we do not consider the viscosity and the thermal conductivity in our model in order to study the artificial diffusion effect deriving for the numerical schemes.
The domain is constituted of a gas and several copper inductors $I_1, \ldots, I_K$ powered by a voltage supply V_k, $k = 1, \ldots, K$ (See Fig. 1: right) prescribed on a cross–section S, located at $\theta = 0$ on the inductors.

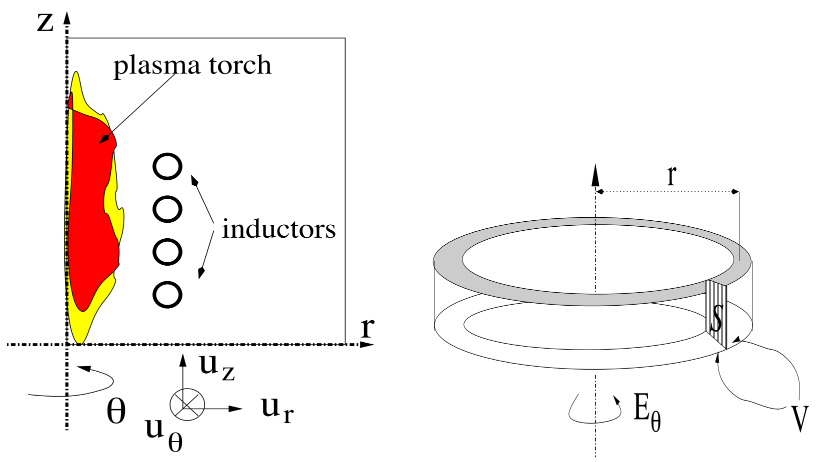

Figure 1: A simple plasma torch: geometrical conventions (left). Voltage on surface S in the inductor (right).

Assembling all these considerations, eddy current equations result in the following partial differential equation satisfied by the azimuthal component of the electric field:

$$-\frac{\partial}{\partial r}\Big(\frac{1}{r}\frac{\partial}{\partial r}(rE_\theta)\Big) - \frac{\partial^2 E_\theta}{\partial z^2} + i\omega\sigma\mu_0 E_\theta = \frac{i\omega\mu_0\sigma}{2\pi r}\sum_k V_k\ \mathbb{1}_k(x), \tag{1}$$

where $\mathbb{1}_k(x) = 1$ if $x \in I_k$ and zero elsewhere, μ_0 is the magnetic permeability of the vacuum and σ is the electric conductivity. It is noteworthy that this equation readily implies the symmetry condition $E_\theta = 0$ on axis $r = 0$, but this condition is not automatically satisfied by numerical schemes and must then by enforced. As far as conditions at the infinity are concerned, E_θ must satisfy the condition

$$E_\theta(r,z) = O\Big(\frac{1}{(r^2+z^2)^{\frac{1}{2}}}\Big) \qquad r^2 + z^2 \to \infty.$$

However, in our computations, this conditions is approximated by choosing a large domain that contains the conductors and prescribing on its boundary the condition

$$\frac{\partial E_\theta}{\partial r} = 0.$$

In the gas, the conductivity $\sigma = \sigma(T)$ depends on the temperature according to the following law:

$$\sigma(T) = \begin{cases} 0 & \text{if } T < 5000, \\ \frac{T-5000}{10} & \text{if } T > 5000. \end{cases} \tag{2}$$

Finally, using the Faraday equation

$$i\omega\mu_0 \mathbf{H} + \nabla \times \mathbf{E} = 0,$$

where $\mathbf{H}$ is the magnetic field, we obtain

$$H_r = -\frac{i}{\mu_0\omega}\frac{\partial E_\theta}{\partial z}, \quad H_z = \frac{i}{\mu_0\omega r}\frac{\partial}{\partial r}(rE_\theta). \tag{3}$$

For the fluid flow problem, we introduce compressible Euler equations in cylindrical coordinates with θ–invariance:

$$\frac{\partial}{\partial t}(r\rho) + \frac{\partial}{\partial r}(r\rho u_r) + \frac{\partial}{\partial z}(r\rho u_z) = 0, \tag{4}$$

$$\frac{\partial}{\partial t}(r\rho u_r) + \frac{\partial}{\partial r}(r\rho u_r^2 + rP) + \frac{\partial}{\partial z}(r\rho u_r u_z) = \rho u_\theta^2 + P + f_r, \tag{5}$$

$$\frac{\partial}{\partial t}(r\rho u_z) + \frac{\partial}{\partial r}(r\rho u_z u_r) + \frac{\partial}{\partial z}(r\rho u_z^2 + rP) = f_z, \tag{6}$$

$$\frac{\partial}{\partial t}(r\rho u_\theta) + \frac{\partial}{\partial r}(r\rho u_\theta u_r) + \frac{\partial}{\partial z}(r\rho u_\theta u_z) = -\rho u_\theta u_r, \tag{7}$$

$$\frac{\partial}{\partial t}(r\mathfrak{E}) + \frac{\partial}{\partial r}(ru_r(\mathfrak{E}+P)) + \frac{\partial}{\partial z}(ru_z(\mathfrak{E}+P)) = s_{\text{jou}} + s_{\text{rad}}, \tag{8}$$

where ρ, $\mathbf{u} = (u_r, u_\theta, u_z)$ and $\mathfrak{E}$ are the gas density, the velocity, the total energy while the pressure P, the internal energy e and temperature T satisfy

$$\mathfrak{E} = \rho\, e + \frac{1}{2}\rho|\mathbf{u}|^2,\ \ P = (\gamma-1)\rho\, e,\ \ e = C_v T.$$

Moreover, the Lorentz-Laplace force $(f_r, 0, f_z)$ and the Joule effect s_{jou} are given by

$$\mathbf{F}_L = \frac{\mu\sigma}{2\omega}\,\mathrm{Re}(\overline{E}_\theta \mathbf{H}_i),\ \ s_{\text{jou}} = \frac{1}{2} r\sigma |E|^2, \tag{9}$$

where $\overline{E}$ is the conjugate function of E, $|E|$ the modulus and Re the real part of a complex number. Note that we do not assume $u_\theta = 0$ since we intend to take the swirl flow into account.
Finally, the radiation phenomenon is included in the model using the net emission approximation [9]. In the present case we use an explicit representation of the radiative emission in function of T given by

$$s_{\text{rad}} = \begin{cases} 0 & \text{if } T < 3000, \\ -10.55\ \exp(T/420) & \text{if } 3000 \le T \le 10000, \\ -4.6\,10^{10}\exp(T/7143) & \text{if } T > 10000. \end{cases}$$

To compute numerical approximation, we use, on the one hand, a $\mathbb{P}_1$ finite element method for electric and magnetic field, and on the other hand we have designed a specific finite volume method coupling with a multislope MUSCL second order technique for the Euler system [7, 8]. The numerical method is detailed in the following sections.

2.2 Geometrical ingredients

In the coordinate system (r, z) we consider a rectangular domain $\Omega = [0, 0.1] \times [0, 0.15]$ with four circular cross-section inductors. The discretization is based on an unstructured mesh $\mathcal{T}$ made of triangles C_i with barycenter B_i, $i \in \mathcal{E}_{el}$ where $\mathcal{E}_{el}$ is mesh element index set (see figure 2). We denote by $j \in \nu(i)$ the index set of neighbour triangles C_j which share a common edge e_{ij} with C_i and $\mathbf{n}_{ij}$ stands for the unit normal vector pointing from C_i toward C_j. Let furthermore

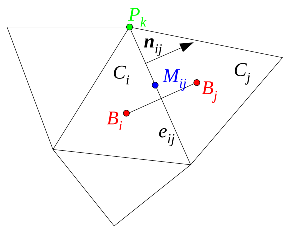

Figure 2: Geometrical ingredients: Cell notation.

P_k, $k \in \mathcal{E}_{nd}$ stand for the set of mesh nodes and $\mathcal{E}_{nd,0} \subset \mathcal{E}_{nd}$ the subset of labels of nodes on the axis $r = 0$. Finally, $\delta(i)$ denotes the index set of the nodes belonging to cell C_i.

2.3 The electric field

Let consider the finite element discrete space

$$\mathcal{V}_h = \{\phi \in C^0(\Omega; \mathbb{C}), \phi_{|C_i} \in \mathbb{P}_1, \phi(0, z) = 0\}.$$

We seek and approximation

$$E_h = \sum_{k \in \mathcal{E}_{nd} \setminus \mathcal{E}_{nd,0}} E_k \phi_k \in \mathcal{V}_h$$

of E_θ such that for any $\phi \in \mathcal{V}_h$, using $r\phi$ as a test function and the boundary condition, we have the weak formulation:

$$\int_\Omega \frac{1}{r} \frac{\partial}{\partial r}(rE_h) \frac{\partial}{\partial r}(r\phi)\, dr\, dz + \int_\Omega \frac{\partial E_h}{\partial z} \frac{\partial \phi}{\partial z} r\, dr\, dz \\ + \int_\Omega i\omega\sigma\mu E_h \phi r\, dr\, dz = \frac{i\omega\sigma}{2\pi} \sum_k V_k \int_{I_k} \phi\, dr\, dz.$$

We then construct a constant piecewise approximation of the magnetic field and electric field on each cells C_j with

$$\mathbf{H}_j = \frac{i}{\mu\omega} \sum_{k \in \delta(j)} E_k (\nabla \phi_k)_{|C_j}, \quad E_j = \frac{1}{3} \sum_{k \in \delta(j)} E_k$$

and a constant piecewise approximation of the Joule heating term $s_{\mathrm{jou},h}$ and the Lorentz force $\mathbf{F}_h$ such that on each cell C_j:

$$s_{\mathrm{jou},j} = \frac{\sigma(T_j)}{2} |E_i|^2, \quad \mathbf{F_i} = \frac{\mu\sigma(T_i)}{2\omega} \operatorname{Re}\left(\overline{E}_j \mathbf{H}_j\right).$$

2.4 The fluid flow

For any function v given on cell C_i and function f given on the edge e_{ij}, $j \in \nu(i)$, we define the weighted mean values:

$$v_i \approx \frac{1}{|C_i|_r} \int_{C_i} vr\, dr\, dz, \quad |C_i|_r = \int_{C_i} r\, dr\, dz,$$
$$f_{ij} \approx \frac{1}{|e_{ij}|_r} \int_{e_{ij}} fr\, ds, \quad |e_{ij}|_r = \int_{e_{ij}} r\, ds,$$

where the weight r deriving from the cylindrical coordinates has to be taken into account in the mean expressions: v_i is an approximation of v at the barycenter B_i while f_{ij} is an approximation of f at the edge midpoint M_{ij} (see figure (2)). The first-order finite volume scheme writes:

$$|C_i|_r U_i^{n+1} = |C_i|_r U_i^n - \Delta t \sum_{j \in \nu(i)} |e_{ij}|_r \mathcal{F}(U_i^n, U_j^n, \mathbf{n}_{ij}) + \Delta t\, |C_i| G(U_i^n), \quad (10)$$

where $U_i^n = (\rho_i^n, \rho_i^n \mathbf{u}_i^n, \mathfrak{E}_i^n)$ is an approximation of the weighted mean values of the conservative variables while $\mathcal{F}(U_i^n, U_j^n, \mathbf{n}_{ij})$ stands for the numerical flux across the edge e_{ij} in direction $\mathbf{n}_{ij}$.
The source term $G(U_i^n)$ represents the geometrical contribution due to the cylindrical coordinates. Note that $|C_i|$ the non-weighted measure of cell C_i. A particular challenging problem to design numerical schemes in cylindrical coordinates is the well-balanced issue due to the presence of geometrical terms (see [8] for a detailed study on the subject).

Second order scheme is achieved substituting the first-order approximations U_i^n and U_j^n with better accurate estimations U_{ij}^n and U^{ji} on both sides of e_{ij} in the flux evaluation. We refer to [7] and [8] for a complete description of the schemes.

A wide variety of numerical fluxes is available in the literature (see [12] for a review on numerical fluxes for the Euler system). The goal of the paper is to show that the choice of the numerical flux is of crucial importance and numerical simulations can provide very different results due to an inadequate flux. In the paper we shall consider two popular numerical fluxes: the Rusanov [11] and the HLLC flux [13]. The first one is very simple to implement, no entropy fixing is required but it is responsible of a large amount of numerical viscosity in the shock vicinity. The second one is also simple to implement and it provides entropic solution approximation. It has been designed to preserve the contact discontinuity and reduce the numerical viscosity effect. Second order technique helps to reduce the numerical diffusion but can not eliminate the intrinsic defaults of the fluxes.

2.5 The couplings

Radiation emission, joule effect and Lorentz-Laplace force are integrated with the classical second-order Strang splitting method. We solve ordinary differential equations both for the impulsion and the total energy source terms[12]. The whole algorithm is the following, let E_h^n, B_h^n and U_h^n be approximations of the electric, magnetic field and the conservative variables of the Euler system respectively.

- We determine the electric conductivity $\sigma(T_h^n)$ and compute the electric field E_n^{n+1}.
- We deduce the magnetic field $\mathbf{H}_h^{n+1}$, the Lorentz-Laplace force $\mathbf{F}_h^{n+1/2}$ and the Joule effect $s_{\text{jou},h}^{n+1/2}$.
- We evaluate the radiation emission $s_{\text{rad},h}^{n+1/2} = s_{\text{rad}}(T_h^n)$.
- We perform a full time step of the Euler system without the source terms (but with the geometrical terms) where we compute $U_i^{n+1/2}$ from U_i^n using (10).
- We add the right-hand side contribution with a simple Forward Euler algorithm in time for each cell C_i:

$$\begin{aligned}
&\rho_i^{n+1} = \rho_i^{n+1/2},\\
&\rho_i^{n+1}\mathbf{u}_i^{n+1} = \rho_i^n\mathbf{u}_i^n + \Delta t F_i^n,\\
&\mathfrak{E}_i^{n+1} = \mathfrak{E}_i^{n+1/2} + \Delta t(s_{\text{jou},i}^{n+1/2} - s_{\text{rad},i}^{n+1/2}).
\end{aligned}$$

We recover the second-order Strang splitting if we perform the first half-step with the right-hand side term using the initial condition.

3 Numerical simulations

Our objective is to show with a simple example that the choice of the numerical flux to solve the same problem can provide two completely different solutions.

We want to emphasize that in the case of complex multiphysics problems, numerical schemes should be used with care to provide a physically representative solution. In the present study, we consider the Rusanov and the HCCL numerical solver and their impacts on the approximation whereas all the other numerical schemes (finite elements for the electric and magnetic field, Strang splitting for the source terms) are the same: the different behaviour have to be attributed to the Riemann solvers.
To perform the numerical tests, we consider a simple torch in axisymmetric geometry depicted in figure 3 where we use a Delaunay mesh with 22096 elements and 10985 nodes.
The initial condition correspond to a gas at rest with a uniform pressure $P_{ini} = 10^5\,Pa$. The red area is the ignited plasma where we set a uniform density

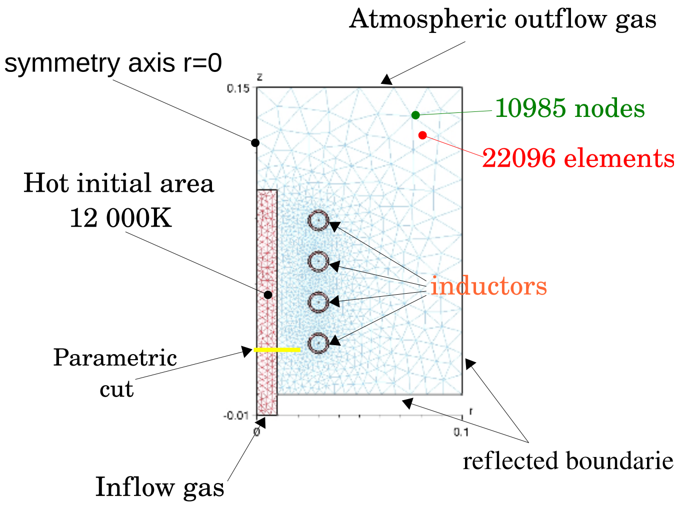

Figure 3: Mesh and boundary conditions.

$\rho_p = 0.003$ corresponding to a temperature of $T_p = 12\,000\,K$ whereas the blue area the gas with density $\rho_2 = 1.2$ which corresponds to the room temperature $T_2 = 300\,K$.
We use reflection conditions for the two vertical sides and the bottom of the rectangular while we use a transmission condition for the top side of the domain while we set the homogeneous Neumann condition on whole boundary for the electric field.

3.1 First run: $V_k = 0$

In the first test, we assume that there is no current in the inductors and the radiation emission is set to zero to avoid the plasma cooling. We then face to a classical Riemann problem at the interface between the hot and the cold gas. Since we do not have any thermal diffusion and the pressure is uniform, the solution corresponds to the initial state where the hot and cold areas are preserved.

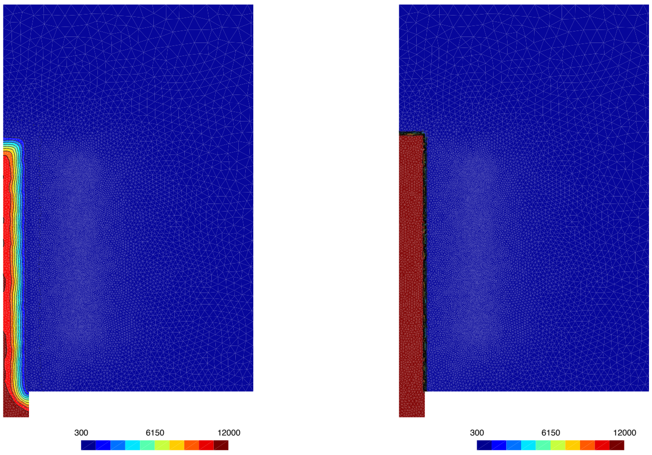

Figure 4: Temperature of the plasma torch after $50\,\mu s$ with a $0\,V$ voltage: Rusanov (left) and HLLC (right). The contact discontinuity is well-preserved with the HLLC numerical flux while the too dissipated Rusanov flux rapidly makes uniform the temperature.

Figure 4 shows the temperature distribution of the torch after about $50\,\mu s$. Clearly the Rusanov scheme presents an important numerical diffusion while the HLLC succeeds in preserving the contact discontinuity. The Rusanov numerical flux contains, by essence, a diffusion term for stability reason. In the present simulation, the density discontinuity is very important (0.03 in the hot area and 1.2 in the cold area) and a small transfer of matter into the lower density zone has a great impact on the temperature variation (remember that T acts as $\frac{1}{\rho}$). In few μs, the diffusion is responsible of a density doubling in the vicinity of the contact discontinuity which results in a temperature drop.

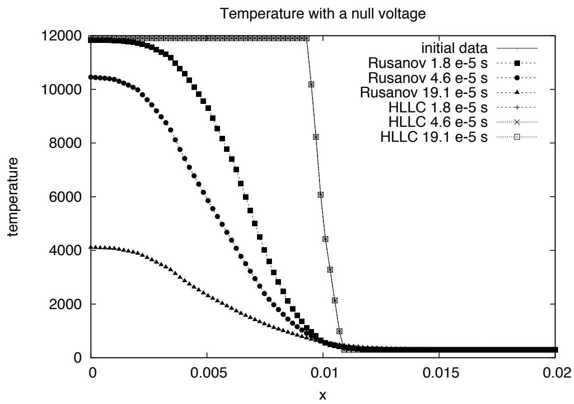

Figure 5: Temperature cut of the plasma torch with a $0\,V$ voltage.

We print out in figure 5 a cut of the temperature at $z = 0.05$ on the interval $[0, 0.02]$ (see figure 3 for the cut location) at the initial time and times $t = 18\mu s$,

$t = 46\mu s$, $t = 191\mu s$. We observe that the HLLC numerical flux allows a nice contact discontinuity preservation while the Rusanov flux switches off the plasma since we reach a temperature lower that $5000\,K$ (corresponding to a null conductivity) after about $200\,\mu s$.

3.2 Second run: $V_k = 1500\,V$

We now impose a voltage of $1500\,V$ in the four inductors to create a electric field which induces eddy current inside the plasma while the radiation emission is activated to evacuate the energy. Indeed, without the radiation process, the plasma temperature always increases and no steady-state solution can be achieved.

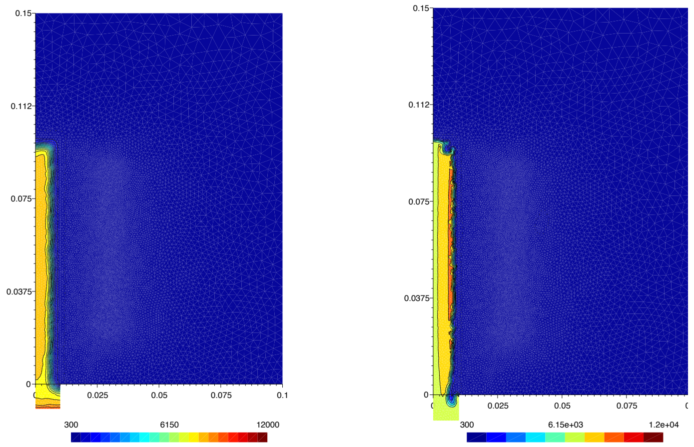

Figure 6: Temperature of the plasma torch after $100\,\mu s$ with a $1500\,V$ voltage: Rusanov (left) and HLLC (right). In the HLLC case, we obtain a steady-state situation which corresponds to balance between the radiation emission and the Joule effect while the Rusanov flux dissipate too much and the plasma will switch off.

Figure 6 shows the temperature distribution of the torch after about $100\,\mu s$. With the HLLC numerical flux, the temperature map reaches an equilibrium corresponding to balance between the radiation emission and the Joule effect. On the contrary, the Rusanov scheme has too much diffused the density leading to a dramatic reduction of the internal energy to reach below the ignition temperature: the plasma switches off after about $200\mu s$.

We draw in figure 7 several cuts of the plasma torch at time $t = 18\mu s$, $t = 46\mu s$ and $t = 191\mu s$. We observe the convergence to the steady-state solution in the HLLC case while the Rusanov flux provides an other solution corresponding to a uniform cold gas. The Joule heating is not enough to compensate the viscosity effect of the numerical flux.

3.3 Third run: $V_k = 2000\,V$

In the last test, we increase the voltage up to $2000\,V$ in the four inductors to obtain a stronger heating of the plasma. We reach to a new steady-state situation

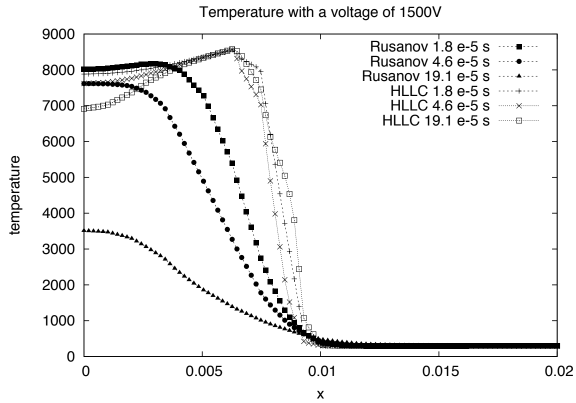

Figure 7: Temperature cut of the plasma torch with a $1500\,V$ voltage.

with the HLLC numerical flux similar to the previous case where the temperatures are slightly higher. On the contrary, the Rusanov flux provides this time a complete different behaviour with a important growth of the temperature. The mechanism is the following: the gas is strongly heating in a small layer at the periphery of the plasma. Due to the large diffusion of the scheme, matter in cold zone flows into the hot zone in the vicinity of the contact discontinuity but, this time, the cooling is compensated by the Joule effect. Moreover, the initial cold zone warms up until it reach the ignition temperature. Consequently the plasma zone increases (cold area turns to be hot area) and the torch rapidly inflates till it touches the inductors.

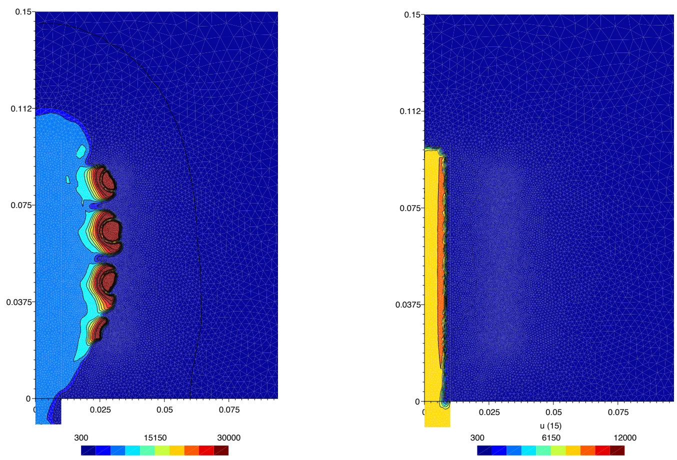

Figure 8: Temperature of the plasma torch after $400\,\mu s$ with a $2000\,V$ voltage: Rusanov (left) and HLLC (right). The HLLC flux provides a new steady-state solution while the torch inflates with the Rusanov numerical flux.

We draw in figure 9 several temperature cuts at $t = 284\mu s$, $t = 377\mu s$ and $t = 470\mu s$. We clearly observe the steady-state situation with the HLLC scheme whereas the torch inflation with a mean temperature of $7800\,K$ is obtained.

When the torch gets closer to the inductor, a huge current Joule effect is generated and we observe temperatures up to $50\,000\,K$ around the inductors.

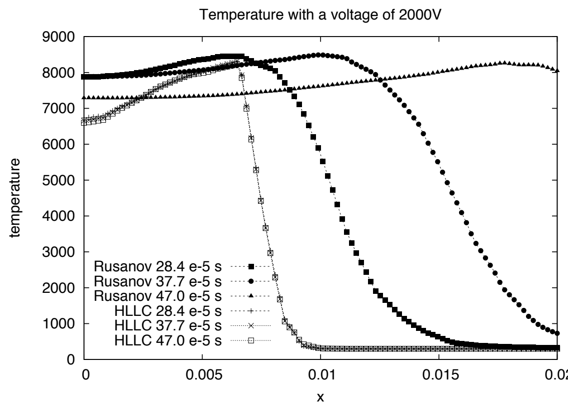

Figure 9: Temperature cut of the plasma torch with a Voltage of $2000\,V$.

4 Conclusion

To perform plasma torch numerical simulation, we have to face a complex multiphysic problem where both finite element and finite volume methods are employed. We show with simple examples the impact of the numerical scheme choice where we have detailed three representative situations. It comes that due to the numerical viscosity, simulations carried out considering the Rusanov or HLLC numerical fluxes provide completly different numerical solutions for the exactly the same physical problem. A blind usage of numerical solver can lead to non relevant physical solutions.

References

[1] D. Vacher Détection, en temps réel, d'éléments métalliques présents dans les rejets atmosphériques industriels par torche à plasma à couplage inductif, Ph.D. Thesis (in French), Université Blaise Pascal, Clermont–Ferrand, 2001.

[2] G. Herdrich, M. Auweter-Kurtz, P. Endlich, Mars Entry Simulation using the Inductively Heated Plasma Generator IPG4, Journal of Spacecrafts and Rockets, Vol. 40, No. 5, (2003) 690–694.

[3] A.F. Kolesnikov et al., Study of quarts surface catalycity in dissociated carbon dioxide subsonic flows, Journal of Spacecraft and Rockets, Vol. 37, No. 5, (2000) 573–579.

[4] D. Vacher, M. Lino da Silva, P. André, G. Faure, and M. Dudeck, Raadiation From an Equilibrium CO_2–N_2 Plasma in the [250–850 nm] Spectral Region: I. Experiment, Plasma Sources Sci. Technol., Vol. 17, 035012, (2008) 1–8.

[5] M. Lino da Silva , D. Vacher, M. Dudeck, P. André, and G. Faure, Radiation From an Equilibrium CO_2–N_2 Plasma in the [250–850 nm] Spectral Region: II. Spectral Modelling, Plasma Sources Sci. Technol., Vol. 17, 035013, (2008) 1–9.

[6] Défi Systèmes, 94 av. du Docteur Fleming, Z.I. St Cézaire, 30900 Nîmes, France.

[7] T. Buffard, S. Clain, Monoslope and multislope MUSCL methods for unstructured meshes, To appear in J. Comp. Phys. 229 (2010), 3745–3776.

[8] S. Clain, D. Rochette, R. Touzani, *Multislope MUSCL method for unstructured meshes applied to the compressible axisymmetric Euler equations for swirling flows*, To appear in J. Comp. Phys. (2010).

[9] A. Gleize, J.J. Gonzales, P. Freton, *Thermal plasma modelling*, J.Phys.D: Appl. Phys. Vol. 38 (2005) R153–R183.

[10] D. Vacher, M. Lino da Silva M., P. André, G. Faure, M. Dudeck, *Radiation from an equilibrium CO2-N2 plasma in the [250-800nm] spectral region: I,II* Experiment Plasma Sources Sci. Technol. 17 8p 035012 (2008).

[11] V.V. Rusanov, Calculation of interaction of non-steady shock waves with obstacles, J. Comput. Math. Phys. USSR, Vol. 1 (1961) 151–179.

[12] E.F. Toro, *Riemann solvers and numerical methods for fluid dynamics. A practical introduction*, Springer-Verlag, Berlin, 1997.

[13] E.F. Toro, M. Spruce, W. Speares, *Restoration of the contact surface in HLL-Riemann Solver*, Shock Waves Vol. 4 (1994) 25–34.